Multi step structural health monitoring approaches in debonding assessment in a sandwich honeycomb composite structure using ultrasonic guided waves

Kaleeswaran Balasubramaniam [a,*], Shirsendu Sikdar [b,c], Rohan Soman [a], Paweł Malinowski [a]

[a] Institute of Fluid Flow Machinery, Polish Academy of Sciences; Department of Mechanics of Intelligent Structures, Fiszera 14 Street, 80-231 Gdansk, Poland
[b] Mechanics of Materials and Structures (UGent-MMS), Department of Materials, Textiles and Chemical Engineering (MaTCh), Ghent University, Technologiepark-Zwijnaarde 46, 9052 Zwijnaarde, Belgium
[c] Cardiff School of Engineering, Cardiff University, The Parade, Queen's Building, Cardiff CF24 3AA, UK

ARTICLE INFO

ABSTRACT

This paper aims to investigate the use of ultrasonic guided wave (GW) propagation mechanism and the assessment of debonding in a sandwich composite structure (SCS) using a multi-step approach. Towards this, a series of GW propagation-based laboratory experiments and numerical simulations have been carried out on the SCS sample. The debonding regions of variable size and locations were assessed using a pre-defined network of piezoelectric lead zirconate transducers (PZT). Besides, several artificial masses were also placed in the SCS to validate the multi-step structural health monitoring (SHM) strategy. The SHM approach uses a proposed quick damage identification matrix maps and an improved elliptical wave processing (EWP) strategy of the registered GW signals to detect the locations of debonding and other damages in the SCS. The benefit of the proposed damage identification map is to locate the damaged area (sectors) quickly. This identification step is followed by applying the damage localization step using the improved EWP only on the previously identified damage sector region. The proposed EWP has shown the potential to effectively locate the hidden multiple debonding regions and damages in the SCS with a reduced number of calculations using a step-wise approach that uses only a selected number of grid points. The paper shows the effectiveness of the proposed approach based on data gathered from numerical simulations and experimental studies. Thus, using the above-mentioned SHM strategy debondings and damages present within and outside the sensor network are localized. The results were cross verified with nondestructive testing (NDT) methods such as infrared thermography and laser Doppler vibrometry.

1. Introduction

Structural health monitoring (SHM) allows fast localization of the damage in the in-service conditions and hence is preferred over the traditional non-destructive testing (NDT) techniques. The guided waves (GW) based SHM techniques have been extensively used for detecting such hidden structural defects [1,2]. GW travel along the structure and may be used for monitoring large areas with relatively few sensors. By identifying the changes in the wave propagation, damage may be detected and even localized. Most of the research papers are based on GW signal difference coefficients [3], time of arrival (TOA) based variation between the healthy and damage signals decomposition [4] and visualizing mode conversion phenomena at the damage [5]. Some

research works focus on analyzing the damage using GW attenuation [6] and dispersion effects [7,8].

Sandwich composite structures (SCS) with honeycomb core and carbon fibre (graphite/epoxy) face sheets are widely used in various industrial applications from aerospace to civil engineering. These SCS are bonded together with strong adhesives to ensure structural integrity. The quality of adhesion of the SCS may be affected by human error [9], improper curing [10], overloading [11] and moisture intrusion [12], among other factors. A significant drop in adhesion quality may lead to the separation of the face sheets and the core adhesive layer at some points [13]. This localized loss of adhesion is referred to as debonding. Early-stage detection of such debonding is crucial for the safe exploitation of SCS. This detection is not possible visually, and NDT methods/
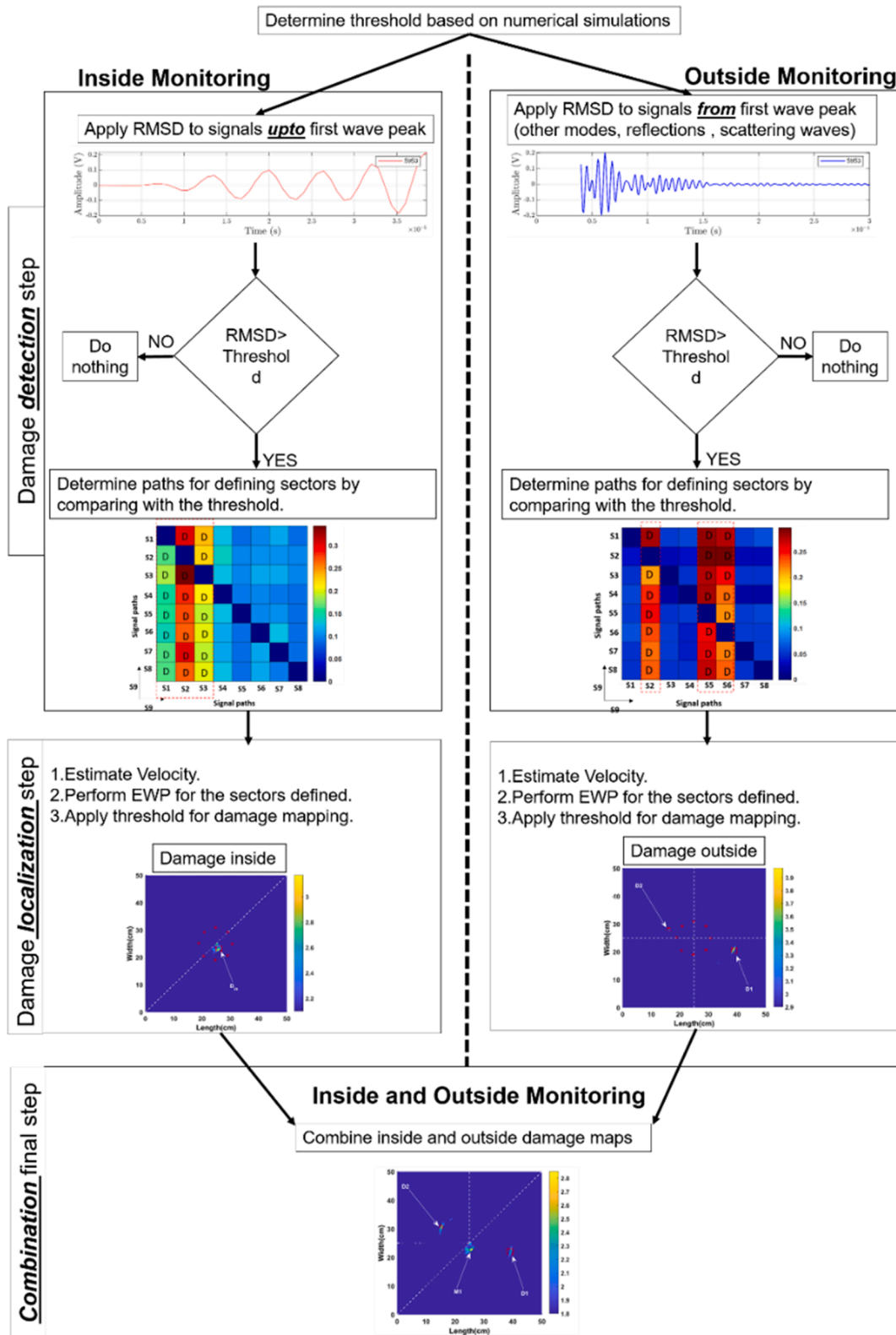
Fig. 1. A methodological flowchart explaining the proposed process.

tools are necessary to determine the structure's safety.

The key challenge with the use of NDT for debond detection is the complexity of the structure. The common problem in the SCS is the interfacial debonding between layers, which was analyzed using different approaches [14]. For the SCS, the GW interference and reflection inside the core region reduce the amplitude [15,16]. The

presence of barely visible impact damage in sandwich structures also strongly influences the amplitude [17,4], and an increase in its size affects the GW propagation [18].

Researchers have carried out debonding detection in honeycomb structures in [19]. The laser Doppler vibrometer (LDV) data was used to visualize the mode conversion phenomena in honeycomb composites
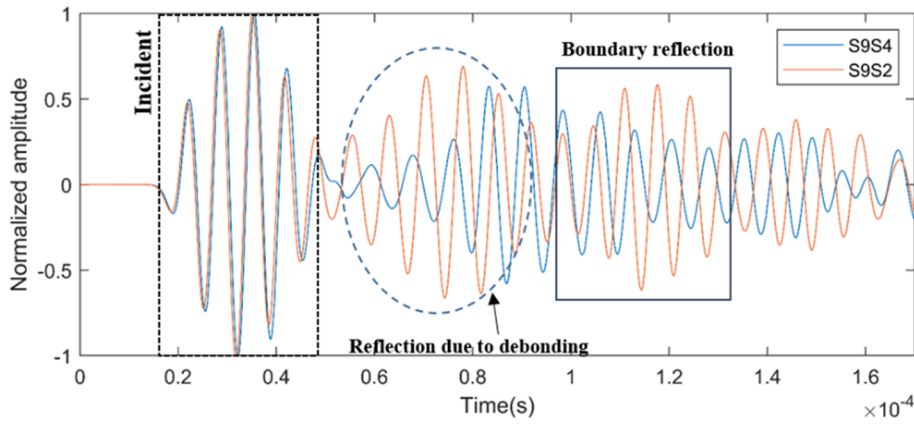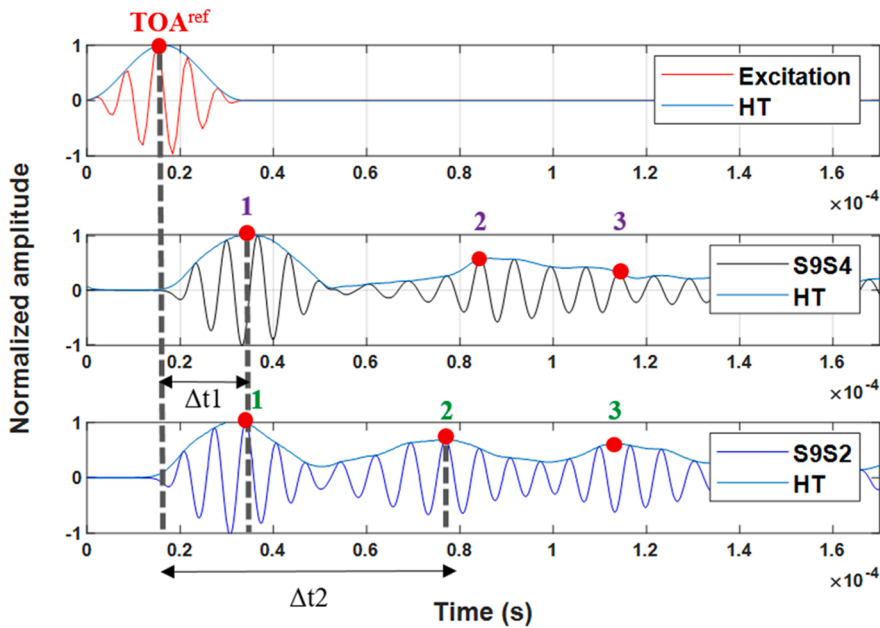
Fig. 2. Signals (150 kHz) showing the incident and reflections.

1,2,…are the TOA^{exp} HT peaks of **S9S4**   1,2,…are the TOA^{exp} HT peaks of **S9S2**

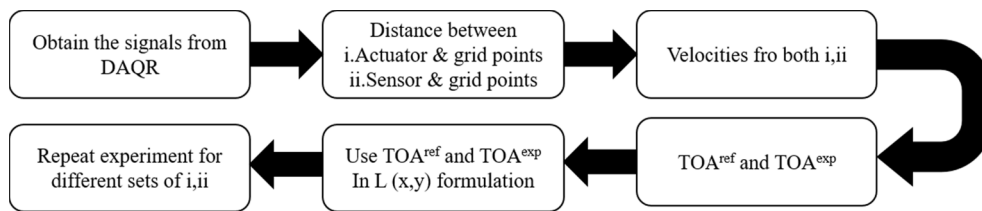Fig. 3. Δt and TOA peak picking calculation between the reference, S9S4, S9S2.

Fig. 4. Flowchart of the EWP process.

[20]. These studies mainly used experimental LDV full wavefield (FWF) measurements to identify the damages and compare them against the healthy structure. Even though LDV based FWF imaging methods identify the damage, it is time-consuming. Most studies involving multi-layered structures use the finite element method (FEM) for gathering damage response and TOA analysis [8]. For all of these analyses, the FEM is used to study the dispersion characteristics and magnitude curves [7,21]. *Castaings et al.* developed a semi-analytical model [22] based on the Thomson Haskell method for predicting the dispersion curves. Researchers also used FEM based stiffened composite models to check the

dispersion behaviour of the GW [23]. These studies used predicted and modelled dispersion curves to show the varying dispersion values between the debond region and the perfectly bonded region. This information may not always be available, thus reducing the efficacy of the proposed methods.

The debond localization was done using the wave filtering approach [24], visualization using root mean square (RMS) based plots [25], damage index (DI) based on signal difference correlation coefficient [2,26–28] and using probabilistic reconstruction approaches [15,29]. The wave filtering approach identified the debond based on the damage
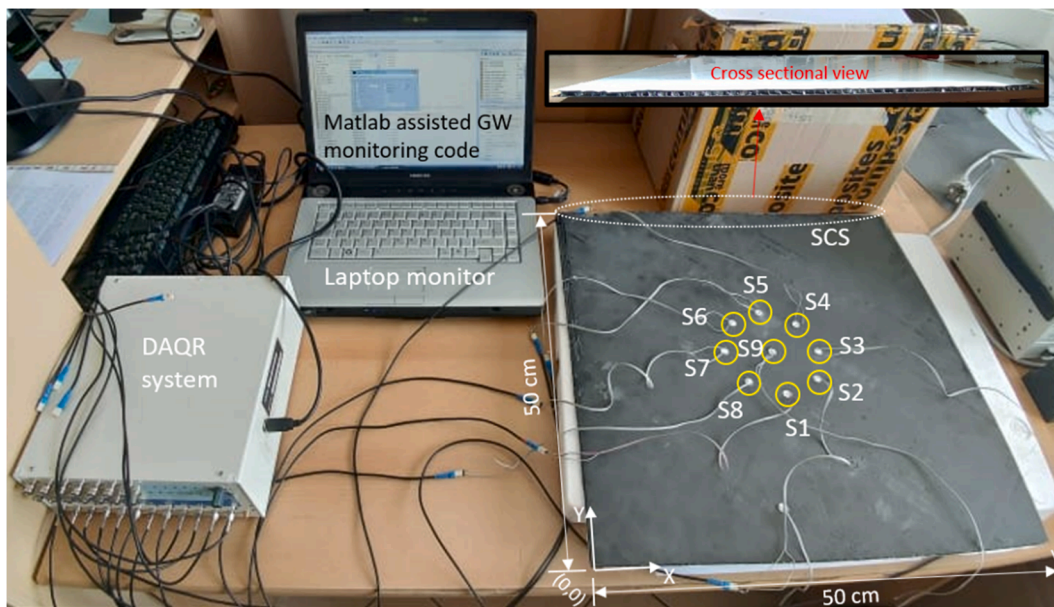
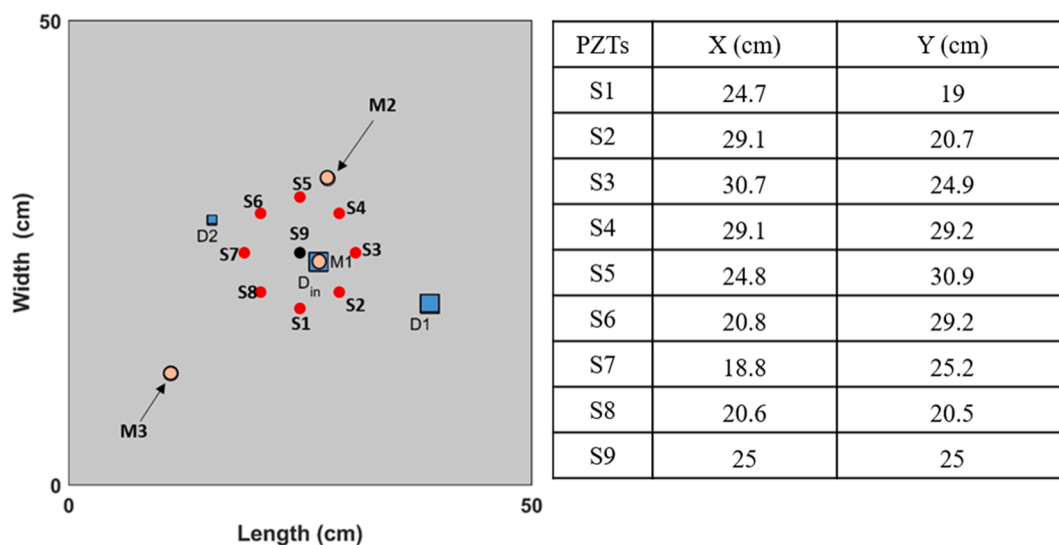**Fig. 5.** Experimental setup for the GW based SHM of SCS using PZTs.

PZTs	X (cm)	Y (cm)
S1	24.7	19
S2	29.1	20.7
S3	30.7	24.9
S4	29.1	29.2
S5	24.8	30.9
S6	20.8	29.2
S7	18.8	25.2
S8	20.6	20.5
S9	25	25

Fig. 6. Schematic representation of the SCS with debonding [square] and artificial masses [M], positions (coordinates of the centre) of PZTs.

Table 1
Experimental cases studied.

Cases	Damages
1	D1 and D2
2	M1 with D1, D2
3	M2 with D1, D2
4	M3 with D1, D2

input from the FWF studies and takes higher computation time. FWF based debond analysis on a composite winglet was studied by *De Luca et al.* [30]. *Perfetto et al.* used an artificial neural network (ANN) based amplitude difference formulation to show the change in the DI by comparing the healthy and damage states [31]. Debond visualization using such DI based studies also follows the same pattern wherein the user mostly requires FWF data for processing. Using time-reversal analysis, probabilistic reconstruction-based schemes debond were analyzed on FEM sandwich beams and experimental plates [32,33].

Sikdar et al. localized debonding in sandwich structures using signal difference based on the modal amplitude area method [34]. A similar localization scheme is used in [35] to locate the debond using linearly placed sensor networks. The debond analysis using the signal difference based coefficient and probabilistic methods can identify anomalies only within the sensor network as their path coverage is significantly less.

The literature study identified that most damage identification and localization methods involve the study of the GW signal patterns throughout the sensor-actuator paths present in the entire structure or study the damage present within the sensor network. Analyzing the DI in all grid points (mesh) increases the overall calculation time. Furthermore, in most literature studies, the location of the debonding was present at a considerable distance from the actuator or sensor. Also, in most studies, the damage location lies at the centre of the structure, which falls under the sensor coverage path. The scenarios where the debonding is very close to the sensor have not been investigated sufficiently. Cases related to analyzing multiple damages (e.g. debonding, impact combined) in the SCS were not studied in detail. A quick DI is
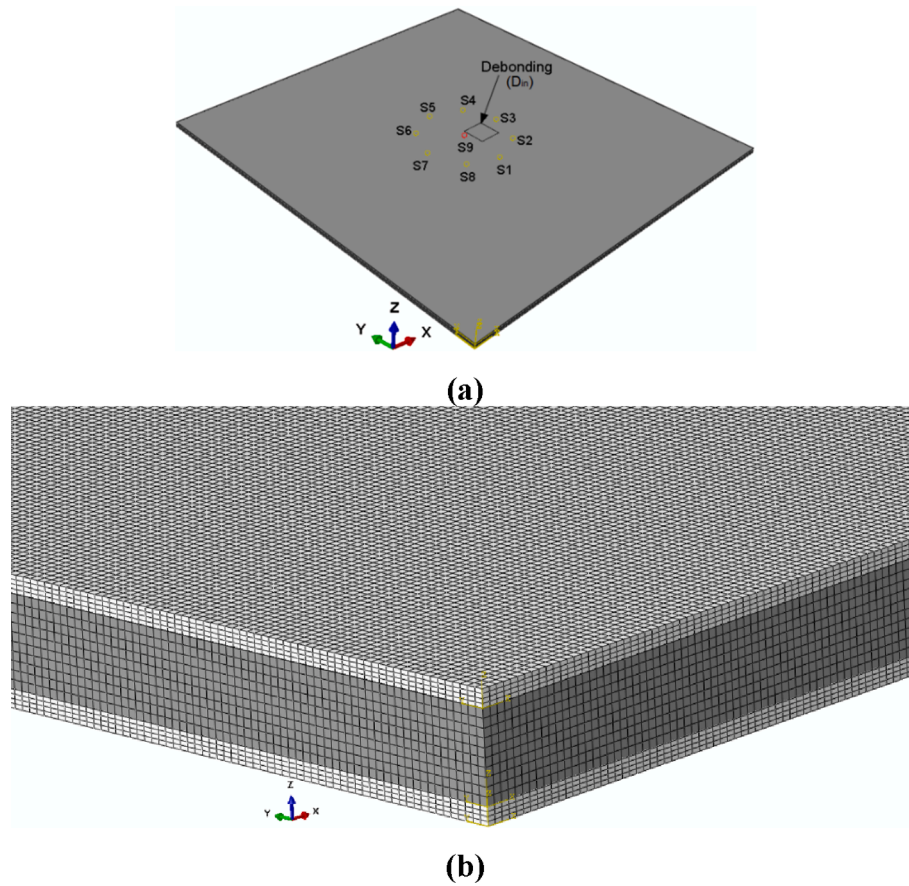
(a)

(b)

Fig. 7. (a) Geometry of the SCS with D_{in}, (b) zoomed view of the meshed model.

Table 2
FEM details used in the modelling.

Type	Part	Element type	Elements number	Nodes number
3D solid	Face sheets	C3D8R	4,000,000	8/element
3D solid	Core	C3D8R	10,000,000	8/element

required to zero-in the damage region in larger system-level structures to carry out local area based NDT applications like infrared thermography (IRT), terahertz spectroscopy (THz) etc.

The study in this paper is motivated to explore and solve the above-mentioned challenging scenarios using a multi-step approach involving damage detection and localization. The research focuses on inspecting the SCS with multiple damages (debonding and artificial mass placements). Debonding of variable sizes and magnets placed at different locations are considered damages in the SCS. A circular sensor network is created to analyze these damages.

The damage detection step helps determine the sectors where damage may be possible. It is done by using a quick root mean square deviation (RMSD) based formulation to locate the regions (i.e. sectors) based on the variation of the RMSD. In the damage localization step, the improved sectorial elliptical wave propagation (EWP) with effective path coverage is applied to sectors identified in the damage detection

step to pinpoint the location of the damage. The approach works to identify the damage locations by taking advantage of the symmetry of the proposed circular network of piezoelectric lead zirconate transducers (PZT) actuator-sensor arrangements. It aims at reducing the calculation time by introducing angular and circular sector-based calculations of the damage indices. The reduction in the calculation time is achieved as the localization step is only applied to the identified sectors and not to the whole model. The code is improved to include the inside and outside localization of damage by taking healthy threshold values, compared to the previous code based on an inner-outer sensor network study and did not consider any healthy threshold-based analysis for

Table 4
Numerical models prepared and studied.

Cases	Models
5	Healthy SCS
6	D_{in}
7	D1, D2
8	D1 alone

where: E1, E2, E3 are Young's moduli, G12, G23, G13 are shear moduli, ν_{12}, ν_{13}, ν_{23} are the Poisson's ratios and 'ρ' is the mass density of the materials.

Table 3
Material properties of the SCS for numerical simulation.

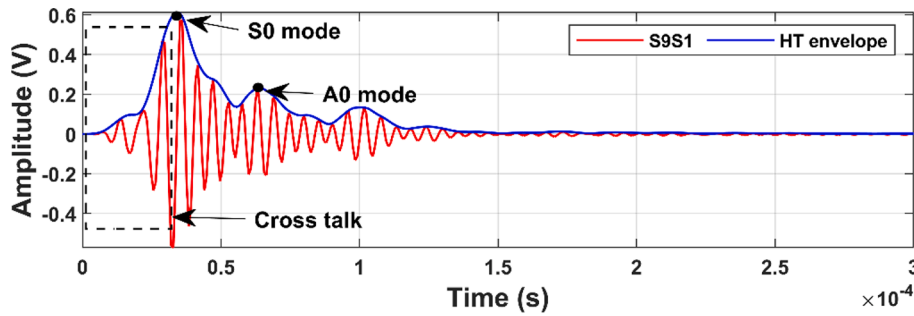| Material	E_1 (GPa)	E_2 (GPa)	E_3 (GPa)	G_{12} (GPa)	G_{23} (GPa)	G_{13} (GPa)	ν_{12}	ν_{13}	ν_{23}	ρ (kg/m^3)
Face	112.0	112.0	19.45	42.50	4.54	4.54	0.30	0.13	0.13	1660
Core	0.099	0.098	1.825	0.043	0.097	0.097	0.26	0.039	0.039	48.50

Fig. 8. Selection of amplitudes from the peak of A0 mode for 150 kHz excitation.
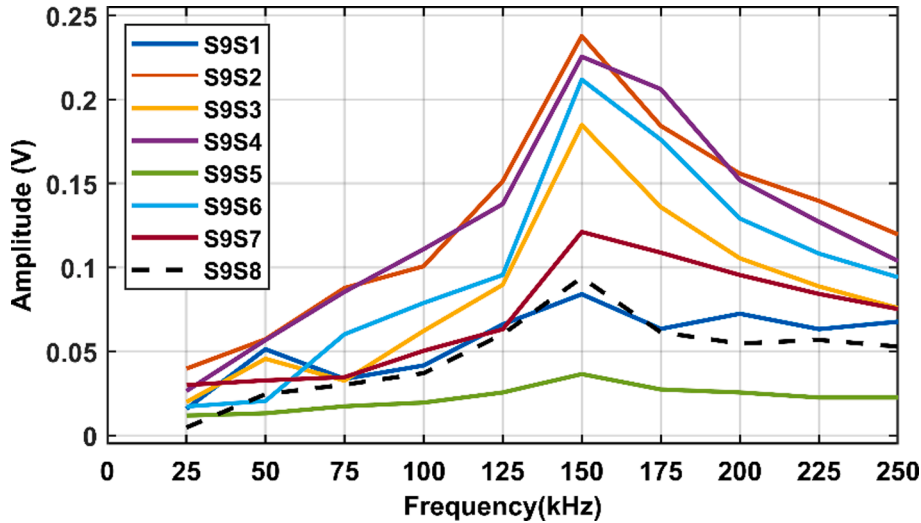

Fig. 9. Amplitude (vs) frequency plot of A0 mode.

Table 5
Velocity values obtained from experimental and numerical data.

Type	V_{S0} at 0°	V_{A0} at 0°	V_{S0} at 270°	V_{A0} at 270°
DAQR-experimental	3432 m/s	2130 m/s	3930 m/s	2586 m/s
ABAQUS-numerical	3481 m/s	2208 m/s	3822 m/s	2497 m/s

obtaining sectors [36]. Thus, damages near the actuator, far from the actuator and multiple damages were successfully localized using the localization step. Numerical models using FEM-ABAQUS© were also prepared to study the multi-step approach with a healthy model and different damages scenarios similar to experimental studies.

The proposed multi-step approach reduces the number of calculations since only the precise localization is conducted in sectors with the identified damage. It is observed that the proposed SHM strategy can effectively locate the hidden debonding regions and damages in the SCS. The SHM results were also cross-checked using IRT and LDV.

2. Methodological overview

To analyze the damage present inside and outside the sensor network, a multi-step SHM process is proposed in this paper. A graphical methodological illustration of the procedure is shown in Fig. 1. A circular arrangement of 9 PZTs (1 actuator, 8 sensors based configuration) forms the sensor network.

1. Damage detection step: It is employed to verify if the damage is inside and/or outside the network. The detection is done by comparison against a threshold value that is determined from numerical simulation.

2. Damage localization step: EWP based localization is utilized for
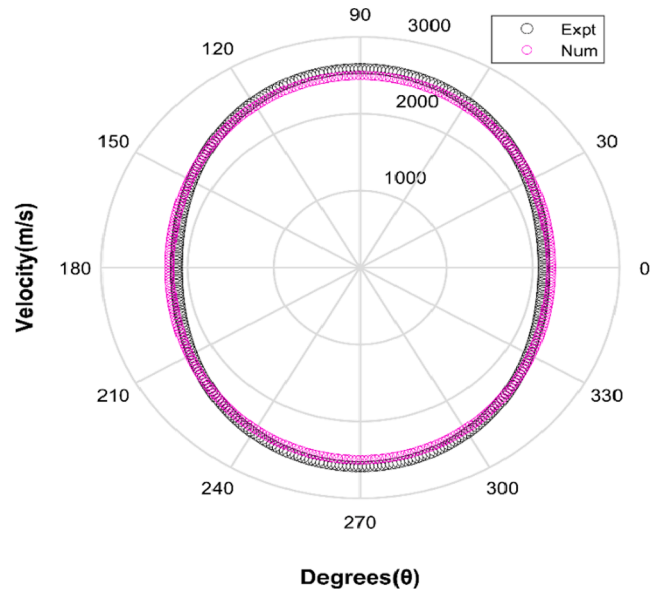

Fig. 10. Velocity profile based on values from Table 5.

obtaining the damage coordinates in the determined sectors.

3. Combination step: The outputs of inside and outside monitoring are merged in this step. If no damage is detected inside, the output is outside the localization result and *vice versa*.
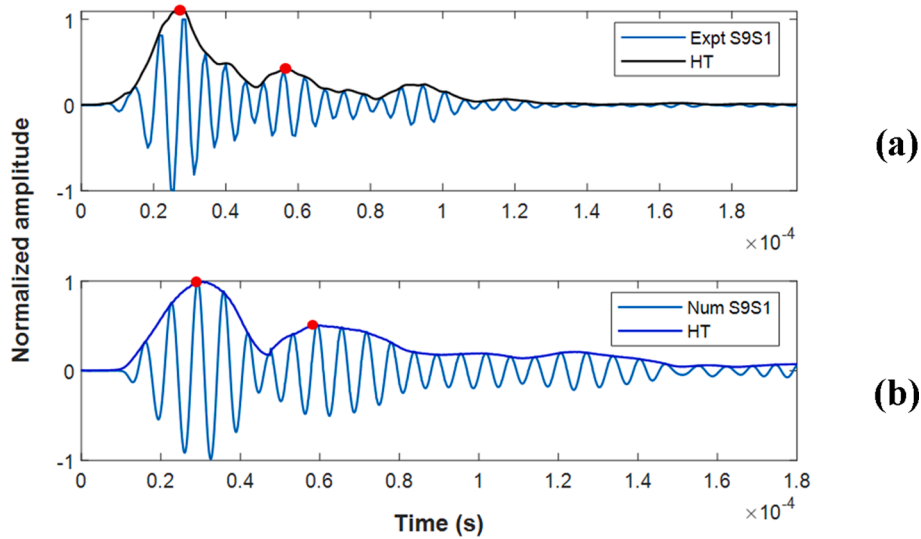
Fig. 11. GW signals corresponding to the path S9S1 from (a) experiment and (b) simulation.
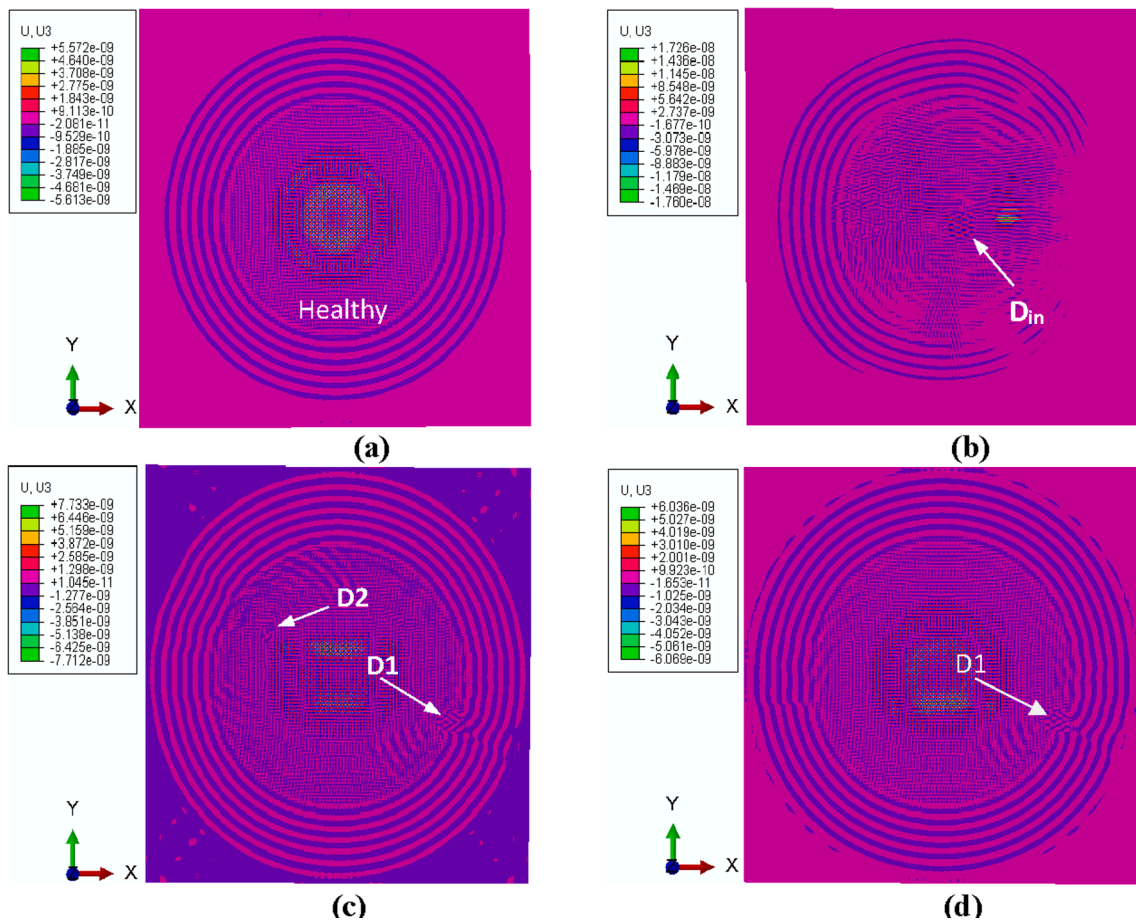

Fig. 12. Numerical wavefield plots (a) Case 5 (b) Case 6 (c) Case 7, (d) Case 8.

2.1. Damage detection step overview

The damage detection step is done using the root mean square deviation (RMSD) formulation as shown in equation (1) which uses the signal up to the first wave peak (inside monitoring) to determine if the damage is inside the sensor network. The wave packets were identified based on the time cut off TOA values obtained from the measured velocity values. The same RMSD equation is used with the complement of signals (outside monitoring) to detect the outside damage.

$$RMSD(i,j) = \sqrt{\frac{\sum\limits_{k=1}^{N}\left(S_i(k) - S_j(k)\right)^2}{\sum\limits_{k=1}^{N}\left(S_j(k)\right)^2}} \tag{1}$$
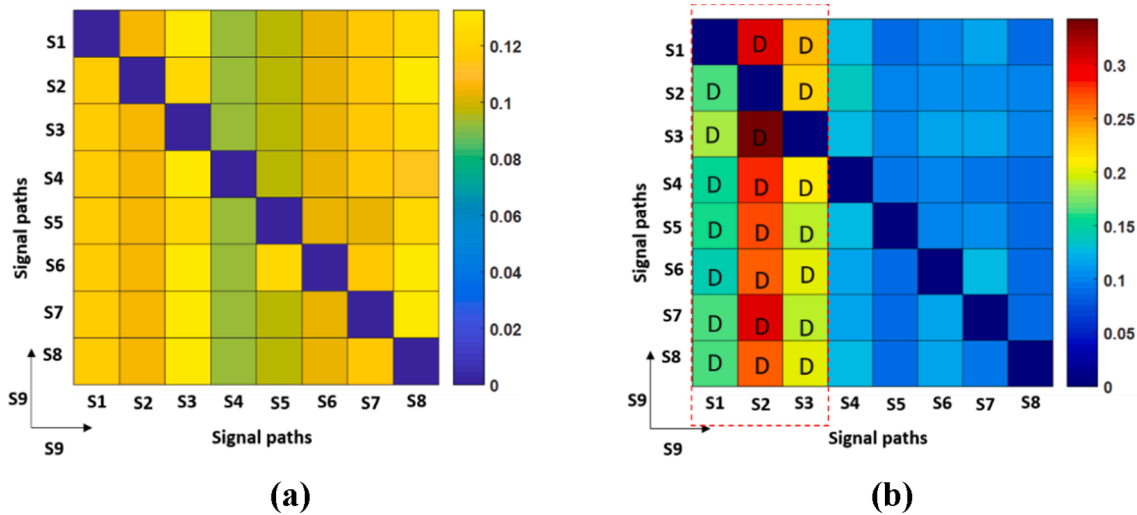
Fig. 13. Damage detection step for inside monitoring: numerical results (a) Case 5 - threshold, (b) Case 6.

Table 6
Damage detection step for inside monitoring: numerical results.

Case	Figure	Higher RMSD columns	Identified damage
5	13(a)	Threshold for cases 6,7,8	–
6	13(b)	S9S1,S9S2,S9S3	D_{in}

where: 'k' is the time samples starting from 1 till N; and S_i and S_j are signals from the 8 sensors after excitation using the S9 actuator ($i.j \in [1, 2,3,\cdots,8]$; $i \neq j$). The code calculates the matrix RMSD, of size 8×8, with 64 signal combinations as inputs. After plotting the RMSD damage index plot, it allows the determination of the zone in which damage is located. Based on the RMSD values, damage and healthy paths are detected by comparison with the threshold values obtained from numerical simulation. Subsection *5.3.1* and *5.4.1* explains the damage detection step results in detail.

2.2. Damage localization step overview

The EWP method is used with a sectorial approach in finding the damage coordinates in the identified paths. A SHM strategy is proposed that uses the time of arrival (TOA) based EWP algorithm on locating the damaged regions in the targeted SCS. The technique uses ellipse based intersection and the coincidence method to highlight the wave reflections corresponding to the damage regions. An exemplary Fig. 2 shows the S9S4 signal path and S9S2 signal path with reflections.

The concept behind the EWP is explicitly described in [37,38] and is further improved in the present paper for sector-wise localization strategy. In the process, the EWP output is assigned to grid points. The number of grid points influences the smoothness of visualization and computational time. In this investigation, fine horizontal and vertical mesh grid steps of $dx = dy = 0.1$ mm are set for result visualization. This method is followed by calculating the theoretical time of arrival termed as TOA^{ref} (equation (2)) for the waves to travel from the actuator to an arbitrary grid point and then to the sensor.

$$TOAref = \frac{\sqrt{(B_x - A_x)^2 + (B_y - A_y)^2}}{V_A} + \frac{\sqrt{(B_x - S_x)^2 + (B_y - S_y)^2}}{V_S} \quad (2)$$

where: B_x, B_y are the grid point coordinates, A_x, A_y are the actuator coordinates, S_x, S_y represents the sensor coordinates, V_A and V_S represents the wave group velocities from the actuator to the grid point coordinates, and from the grid points to the sensor respectively. The group

velocities (V) are calculated based on equation (3).

$$V(m/s) = \frac{\Delta x}{\Delta t} \quad (3)$$

where: Δx is the distance between the sensor locations and Δt is the time distance between the maximal peak values of the excitation signal (e.g. Fig. 3) and the maximal peak value of other signals obtained from the data acquisition and receiver (DAQR). The Hilbert transformation (HT) envelope is applied to the measured signals, and various amplitude peaks are obtained from it. The peaks are then arranged in the ascending order of magnitude (1, 2…). The TOA^{ref} is then correlated with the obtained peak values, as shown in Fig. 3. A higher value in the grid location is identified when the TOA^{ref} agrees with the peak location (TOA^{exp}) identifying the damage region. An exemplary calculation of Δt and TOA (reference, experiment) correlation between the excitation signal, S9S4 and S9S2 signals are shown in Fig. 3 for an exemplary 150 kHz frequency.

The formulae for the debonding localization (equation (4)) is improved to suit the arrival time of varied signals [39].

$$L(x,y) = \sum_{n=1}^{AS} exp[-\frac{|TOA^{ref} - TOA^{exp}|}{\tau}] \quad (4)$$

where: L (x, y) denotes the localization index, AS refers to all the actuator sensor paths used, and TOA^{exp} is the time of arrival obtained from peak values of the experimental data signals. The decay factor τ with a value of 5 µs is used as per the literature [38] for both anisotropic and orthotropic material types. The simplified flowchart of the EWP process is shown in Fig. 4. Subsection *5.3.2* and *5.4.2* explains the damage localization step results in detail.

3. Experimental setup for NDT and SHM studies

The GW study used PZT for exciting and sensing the waves. The PZT disc (1 cm dia., 0.1 cm thin) was procured from Ceram Tec [40] and made from SONOX P502 material. The laboratory experiments on a sample SCS (50 cm × 50 cm × 0.7 cm) have been carried out using a DAQR setup [41]. The setup was complete with 13 channels and is connected to a computer by a USB cable. A MATLAB code controls the device, allowing choosing the type of signal window, excitation frequency, number of cycles, and number of channels to be used. The experimental setup with DAQR-system, sample SCS, cross-sectional view, and a network of PZTs are shown in Fig. 5.

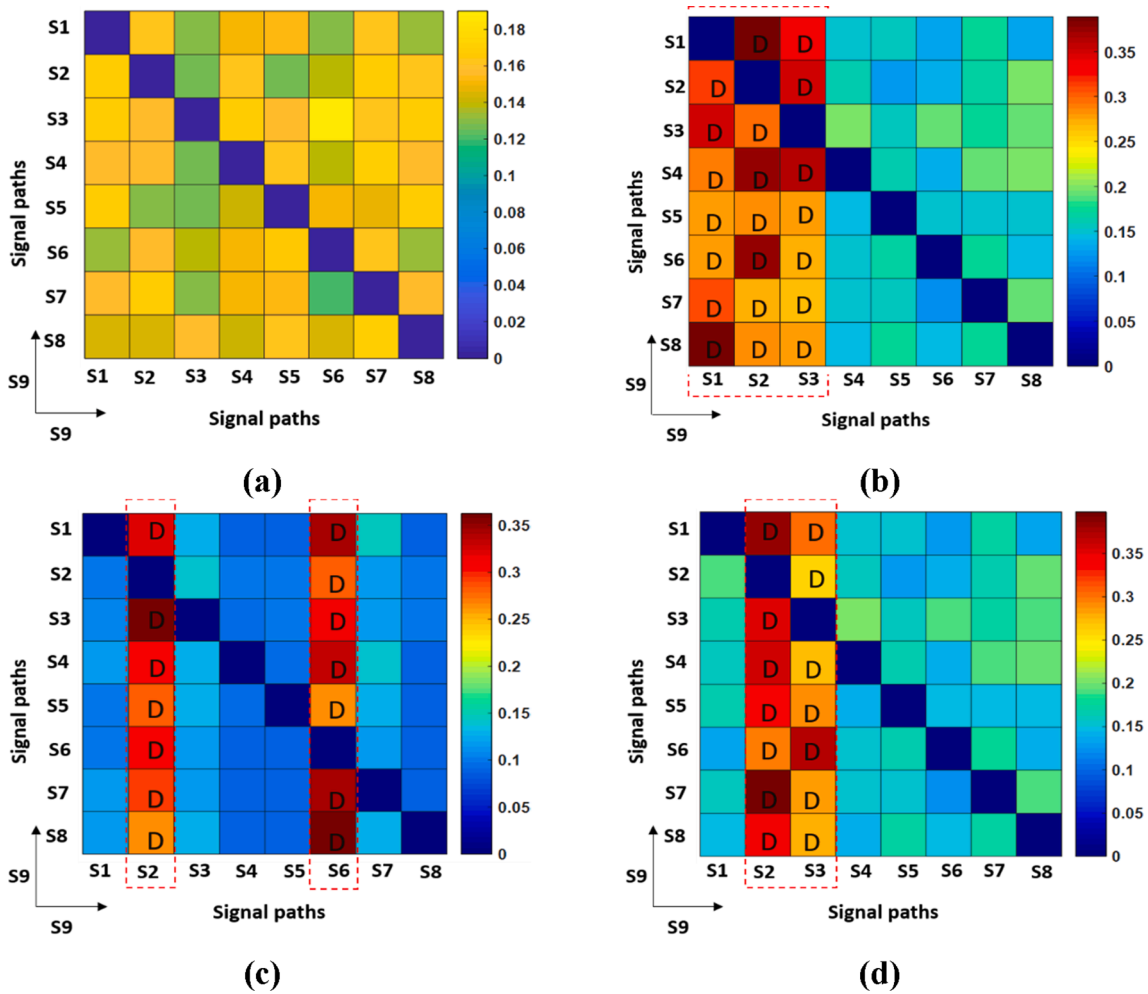The SCS honeycomb core of thickness of 0.5 cm is made of

Fig. 14. Damage detection step for outside monitoring: numerical results (a) Case 5, (b) Case 6, (c) Case 7 and (d) Case 8.

Table 7
Damage detection step for outside monitoring: numerical results.

Case	Figure	Higher RMSD columns	Identified damage
5	14(a)	Threshold for cases 6,7,8	–
6	14(b)	S9S1,S9S2,S9S3	D_{in}
7	14(c)	S9S2, S9S6	D1, D2
8	14(d)	S9S2, S9S3	D1

aluminium with a cell size of 1/8 inches. The 0.1 cm thin CFRP laminates (layup $0°$ /$90°$)$_{3s}$ are used as face sheets bonded to the core by HEXCEL-212Na adhesive. The SCS consists of 2-debondings: D1 (2 cm × 2 cm located at centre coordinates 39 cm, 19.5 cm) and D2 (0.5 cm × 0.5 cm located at centre coordinates 15.5 cm, 28.5 cm). The debonding were introduced during the manufacturing without any adhesive in some regions between the CFRP laminate and aluminium core. In the later part of the experimental study, a magnetic mass (1.5 cm dia and 10 g weight) was placed at three different locations as shown in Fig. 6 as M1 (located at the centre coordinates 27 cm, 24 cm), M2 (located at the centre coordinates 30 cm, 33.5 cm) and M3 (located at the centre coordinates 12 cm, 12.5 cm). Table 1 shows the experimental cases studied.

The SCS was placed on a polyurethane thermofoam sheet to prevent any external vibration. The experimental study was carried out by actuating the PZTs with a 5-cycle sine Hanning pulse with 25–250 kHz frequency ranges. The PZT network consists of 9-PZTs bonded to the SCS with a cyanoacrylate-based adhesive. In the network, the 8 PZTs

(sensors: S1 – S8) are arranged in a circular array around a centric PZT (i.e. S9-actuator) with a radial distance of 6 cm. The S9 was used for excitation, while the S1-S8 were used for sensing. The circular arrangement of PZTs is very effective in damage identification, as proposed in [42,43]. Fig. 6 shows the PZT sensor network study performed for the experimentation.

In addition to the above study with DAQR, FWF measurements using Polytec PSV400 © LDV were done to visualize the debonding and study the wave mode associated with the debond identification. The experiment is performed with S9 acting as actuator and with 5 sine cycle Hanning pulse as excitation signal (averaged 10 times). A voltage of 16 V_{pp} (×20 gain amplification) is applied to PZT [44]. A central frequency of 150 kHz was analyzed (optimal central frequency identified with DAQR studies) at a constant room temperature of 21 ± 1 °C. The sampling frequency is set ten times higher than the excitation frequency to respect the Nyquist–Shannon sampling theorem. To filter out frequencies outside the range of the excitation, proper filter cut-off frequency values (100 kHz − 200 kHz) were set in the instrument.

To verify the location of the debonding, an active IRT test with the FLIRSC5600 device was conducted on the sample. The specifications and other technical details can be obtained from the FLIR website [45]. The SCS sample, as shown in Fig. 5, was heated with a powerful heat source (1 kW) halogen lamp from one side and an IR camera captures the thermograms on another side. The lamp was placed close (10 cm) to the SCS and was turned ON/OFF to produce a short thermal pulse. The Altair-Live software was used for the IRT analysis with the digital level (DL) radiation unit. DL is the simplified unit because the temperature (K)
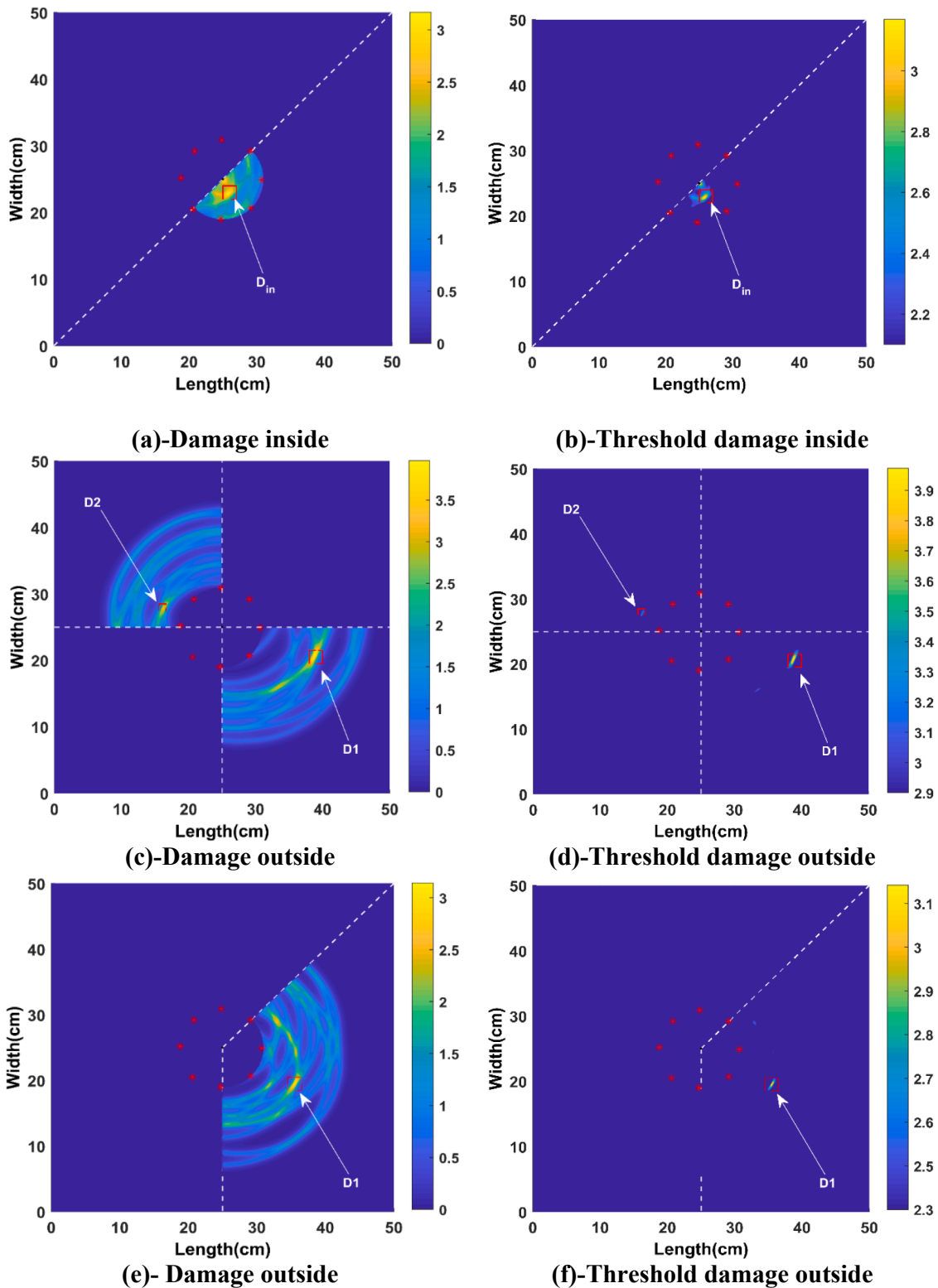
Fig. 15. EWP numerical results: (a) Case 6 (c) Case 7 and (e) Case 8.Threshold of EWP results: (b) Case 6 (d) Case 7 and (f) Case 8.

conversion needs a nonlinear transfer function by knowing the values of transmission, background temperature and emissivity [46]. The IR signals with polynomial represent the thermogram patterns.

3.1. Numerical simulation and extended study cases

FEM-based 3D numerical simulations of GW propagation in SCS

models have been carried out dynamically in ABAQUS to simulate the damage cases. This helped to understand the wave propagation and the wave interactions better. The C3D8R linear-brick elements (orthotropic eight-node 3D, reduced integration and hourglass control) are assigned for the face-sheets (0.05 cm × 0.05 cm × 0.025 cm) and core (0.05 cm × 0.05 cm × 0.05 cm) as shown in [34,47,28]. The core is modelled using C3D8R elements by considering the homogenized orthotropic
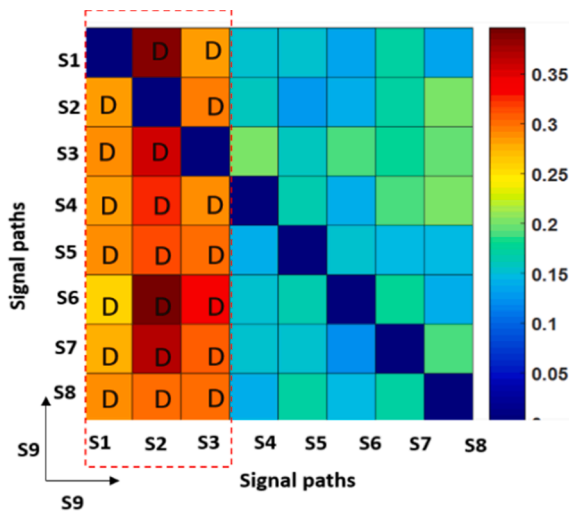
Fig. 16. Damage detection step for inside monitoring: experimental results of Case 2.

Table 8
Damage detection step for inside monitoring: experimental results.

Case	Figure	Higher RMSD columns	Identified damage
2	16	S9S1,S9S2,S9S3	M1

properties. An exemplary FEM geometry model with D_{in} and zoomed region of the meshed model is shown in Fig. 7. A mesh density of 10 elements per wavelength is utilized to capture the GW modes effectively [48]. The elemental size of 0.05 cm (0.5 mm – smallest elemental size L_m) is chosen based on the spatial sampling interval [47–49], aiming to capture the smallest possible wavelength with the L_m. The equation (5) explains the process to obtain the maximum size of the element (L_M) based on the selected velocity of the mode (highest A0 value obtained from experimental case study – denoted as $V_{A0} \sim 2586$ m/s), N = number of elements (10 obtained from literature review) central frequency (150 kHz from experimental studies).

displacement amplitude (meters -m) signals are collected at each sensor location in the sensor network. The dynamic explicit solver considers a stable time increment with time-step 1e-7 (s).

D_{in} (2 cm × 2 cm) located at the centre coordinates 27 cm, 24 cm (as shown in Fig. 6) in Table 4 - Case 6 is a new debonding model (which does not exist in the experiment) to study the proposed multi-step approach for a damage case closer to the sensor network.

4. Results and discussion

4.1. Frequency and velocity determination

This section discusses all the frequencies studied in the experiment and the process of obtaining the desired optimal frequency. The section also highlights the velocity values obtained from the selected optimal frequency and the process of preparing the velocity profile for the damage localization step.

4.1.1. Choice of the frequency and mode

Amplitude values are obtained by picking the maximum peak values of A0 mode for all the frequencies from 25 kHz to 250 kHz measured with DAQR. A0 mode is selected for the study as it identified the debonding (based on the reflection, interference phenomena) when visualized with LDV based GW-FWF studies (results shown in Section 6 -Fig. 20). Another reason is that sometimes S0 mode, due to the higher velocity of propagation, gets mixed up with the initial excitation (cross talk) and was not identifiable in many cases. One example of obtaining the A0 mode amplitude value is shown in Fig. 8 for the S9S1 (excitation at sensor S9 and sensing at sensor S1) with an HT envelope. The amplitude (vs) frequency plot for the actuator S9, sensors (S1-S8) of the entire 25–250 kHz range is shown in Fig. 9.

The amplitude plot shows that the maximum amplitude response is obtained at 150 kHz and is visible with all 8 sensors used. Accordingly, in the further part of the experiment, the 5 cycles, 150 kHz frequency range is chosen as the excitation frequency.

4.1.2. Velocity profile

For the EWP methodology, velocity calculations are required to plot the GW ellipses and for damage localization. The values are obtained from S9S3, S9S1 pairs located at 0, 270° for both experimental and

$$L_M = \frac{V_{A0}}{N \times f} = \frac{2586}{10 \times 150000} = 1.7mm; \; L_m \text{ taken as } 0.5 \text{ mm} \; \sim \; 0.05 \text{ cm (finemesh)} \tag{5}$$

The laminate consists of 10 elements along the thickness and one element per ply. The total number of nodes elements used in the simulation are shown in Table 2.

The material properties considered for the carbon fibre reinforced composite laminate face sheets as per the empirical formula/charts given in [49,50] are presented in Table 3, and the numerical models prepared for the evaluation are shown in Table 4.

A healthy SCS model was prepared with the nodes of the core and the face sheets well connected using surface-bound tie constraints. These tie constraints prevent any relative motion between them. The debondings were modelled by untying the interfacial (core-to-face) nodes at the partitioned debonding regions. The PZT model was omitted in the analysis to simplify the calculations. The GW was excited by applying uniformly concentrated out of plane forces to the respective nodes in place of the actuator. In all simulation cases, the excitation signals are generated through the actuator S9, and the corresponding out-of-plane

numerical signals (Table 5). 0° and 270° (-90°) sensing pairs were used for creating the velocity profile because the CFRP ply orientation is along 0°/90° respectively. The A0 mode wavefield identified the debonding (see Section 6 - Fig. 20), and it is more visible as a separate wave packet at measured time instances (see Fig. 8). Thus, it is chosen as an optimum GW mode, and the velocity values are taken from this mode for the damage localization step.

Similarly, A0 mode velocity calculations are also employed in identifying the debonding in composite SCS [2,15], Aluminium SCS [51]. The uncertainty/changes in the velocity measurements may happen when the sample is tested at higher temperatures conditions [28], positioning and glueing of PZTs [52] etc. These circumstances were avoided by a well-maintained proper room temperature and properly glued PZTs to SCS top skin. The obtained A0 GW mode velocity (V_{A0}) values were then used to calculate the entire 360° values by fitting them with an elliptical function, as shown in Fig. 10. These values were later used in the EWP localization algorithm.
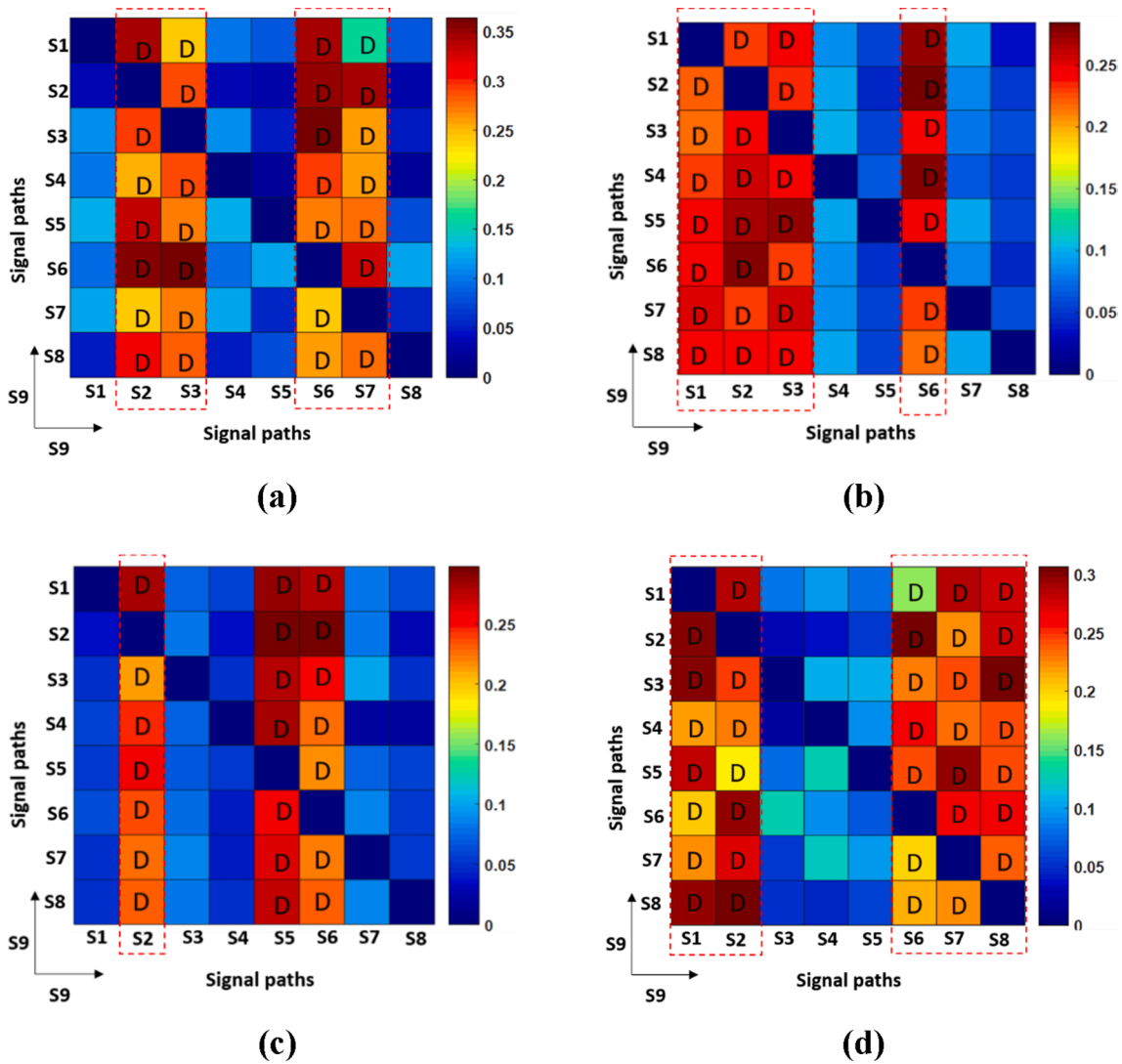
Fig. 17. Damage detection step for outside monitoring: experimental results: (a) Case 1, (b) Case 2, (c) Case 3 and (d) Case 4.

Table 9
Damage detection step for outside monitoring: experimental results.

Case	Figure	Higher RMSD columns	Identified damage
1	17(a)	S9S2,S9S3,S9S6,S9S7	D1, D2
2	17(b)	S9S1,S9S2,S9S3,S9S6	M1,D1,D2
3	17(c)	S9S2, S9S5, S9S6	M2,D1,D2
4	17(d)	S9S2, S9S3	M3,D1,D2

4.2. Validation of the numerical model

The numerical and experimental GW signals (in time-domain) are obtained from all the PZT sensors for different structural conditions with the selected 150 kHz frequency. A general agreement between the experimental and numerical GW signals is observed for all other sensors, in all possible actuator-sensor combinations (exemplary S9S1 signal in Fig. 11).

The time of maxima (red points) of wave mode A0 is almost the same. The experimental case of the SCS has only D1, D2 debondings, as mentioned earlier. A healthy study is not performed as the sample ordered from the manufacturer was with the debonding. But, the advantage of the numerical model is that any possible case study could be performed to visualize it in an actual scenario. This necessitated a numerical SCS study to understand the GW in the healthy state, with D1

located as per the experimental model, D_{in} to check how the GW behaves when damage is within the sensor network, and with both D1 and D2 located as per the experimental model. All these damage cases are visualized at a time step of 8.239 e-5 (s) after excitation (Fig. 12).

Numerical wave field plots corresponding to the out of plane displacements along the Z-direction are shown in Fig. 12. The A0 wavefield plots show the GW propagation and interaction with the debonding. The wavefield plot Fig. 12(a) shows wave propagation in a healthy sample (case 5 – see Table 4). The single debonding D_{in} (case 6) locations, two debonding D1 and D2 (case 7), single debonding D1 (case 8) and their influence on the propagating GWs in the SCS are shown in Fig. 12 (b, c, d).

4.3. Debonding detection- numerical validation

This section discusses the damage detection step for inside and outside monitoring of the numerical cases (5–8), as shown in Table 4. The healthy case (case 5) serves as a threshold for other cases (1–4, 6–8) and all matrix values above the threshold are isolated as probable damage sector regions.

4.3.1. Damage detection step results

Damage detection step overview is the process applied in getting RMSD matrix maps. The RMSD analysis was carried out to identify the
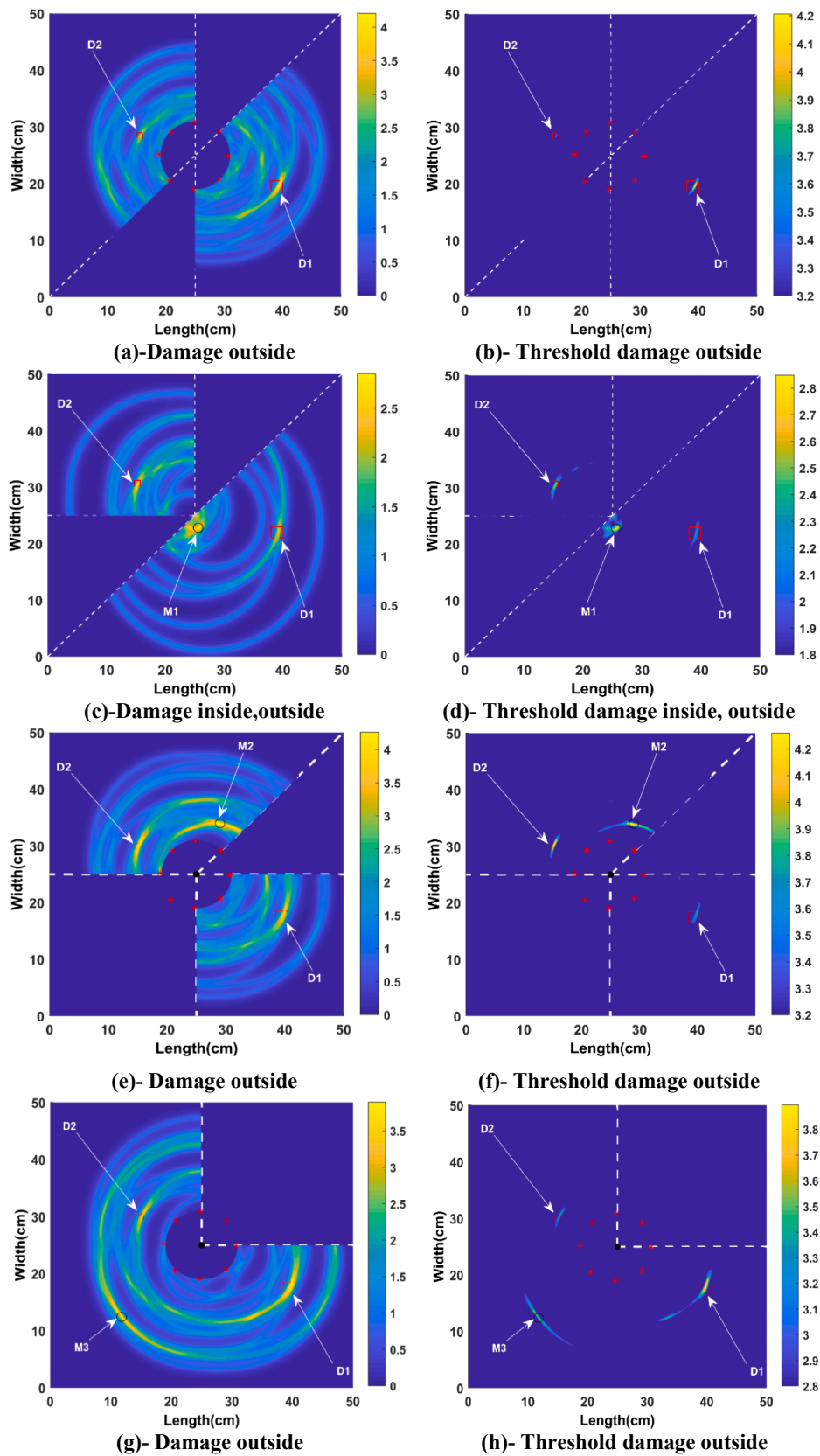
Fig. 18. EWP experimental results: (a) Case 1, (c) Case 2, (e) Case 3, and (g) Case 4.Threshold of EWP results: (b) Case 1 (d) Case 2, (f) Case 3 and (h) Case 4.

Table 10

Comparison table for experimental cases: the EWP damage location identification and error estimation [all units in cm].

Case	EWP D1	EWP D2	EWP M1	EWP M2	EWP M3	$\Delta PD1$	$\Delta PD2$	ΔP M1	$\Delta PM2$	ΔP M3
1	40.1,20.3	16.9,29.3	–	–	–	1.3	1.6	–	–	–
2	38.8,21.1	15.2,29.4	26.6,22	–	–	1.6	0.9	1.4	–	–
3	39.6,17.9	14.8,29.0	–	29,34	–	1.7	0.8	–	1.1	–
4	39.8,17.8	15.0,29.8	–	–	11.6,12	1.8	1.3	–	–	0.8

Table 11

Comparison table for experimental cases: grid reduction in [%], time taken (TT) in mins.

Case	Grids without sectors	Grids with EWP	Reduction in grid points	TT without sectors	TT with EWP
1	251,001	179,992	28.29	13.1	8.5
2	251,001	201,052	19.89	12.6	8.9
3	251,001	150,227	40.14	12.9	6.8
4	251,001	179,594	28.44	13.4	8.3

Table 12

Comparison table for numerical cases: the EWP damage location identification and error estimation [all units in cm].

Case	EWP D1	EWP D2	EWP D_{in}	ΔP D1	ΔP D2	ΔP D_{in}
6	–	–	26,22.8	–	–	1.56
7	38.5,20.5	16.5,29.1	–	1.11	1.16	–
8	39.6,17.9	–	–	1.92	–	–

healthy wave paths and debonding influenced paths. The idea behind the study is to point out which is the actual damage path pair region and which path is closer to the damage than the other signal paths. This method provided a quick and easy analysis of the damage paths and showed effective identification of the approximate damage region. As mentioned earlier, S9 is the actuator in all these cases (S1-S8 acts as sensors). The results obtained by considering the inside monitoring step are shown in Fig. 13 and Table 6.

RMSD matrix map values above the threshold values (0.12) are marked with the letter 'D'. Cases 7,8 matrix maps showed similar values and are below the threshold and show that no further damage is inside the sensor network.

After performing the inside damage detection, the numerical models are checked using the outside monitoring step to detect the existence of any damage region outside the sensor network. An increase in RMSD value for the signal paths that are closer to the debonding indicates the occurrence of changes in signals. Fig. 14 and Table 7 show the RMSD values obtained for numerical ABAQUS data based on the damage detection step for outside monitoring.

RMSD matrix map values above the threshold values (0.18) are marked with the letter 'D' as shown in Fig. 14 (b, c, d). The damage detection step determines the sectors for performing the EWP-based damage localization. The sector for applying the EWP is determined with 45° precision equal to the angular separation of the sensors on the circumference. For instance, if the S9S2 path was identified, the sector borders are defined at the neighbouring sensors (S1 and S3). Whereas if the damage is detected within the sensor network, the sectors within the identified paths and the sensor network are considered (as shown in Fig. 15a as a circular sector).

4.3.2. Damage localization step results

The numerical EWP results for the identified sectors (Fig. 14(b,c,d))

are shown, indicating the location of debondings by intersecting ellipses (Fig. 15). Such higher energy occurs due to the reflection from the debonding. Analysis of Fig. 15 shows the region of higher energy obtained due to the intersection of the ellipses. Case 6 (Fig. 15a) identifies the D_{in} by utilizing combined sector schemes (angular and circular), followed by case 7 (Fig. 15c), identifying both D1, D2. Case 8 shows the EWP result of D1 alone (Fig. 15e). A threshold percentage value of 75 % is applied to sector Fig. 15(a, c, e) to show only the damage locations in Fig. 15 (b, d, f). The threshold value was chosen based on miss-hits and threshold calculations as shown in [5] and also explained in detail in *Appendix A1*.

4.4. Damage detection- experimental validation

This section discusses the damage detection step of the experimental cases (1–4) studied. The experimental case consists of the debondings (case 1-Table 1) in the initial state. Three cases with artificial mass placements are added (cases 2, 3, 4) to further evaluate the proposed multi-step methodology.

4.4.1. Damage detection step results

The results seen in the experimental case study (Fig. 16 and Table 8) tend to show similarity with the results of the numerical case study (Fig. 13b). The matrix map shows only M1 in the case 2 experimental models because only the inside monitoring methodology is applied (cut of signals up to first peak maximum), and thus only M1 gets detected in the inner sensor network region. The numerical case 5 (Fig. 13a) also acts as a threshold for the experimental result (Fig. 16).

In case 3,4 the matrix maps showed similar values below the threshold values and thus assumed no damage is inside the sensor network.

Similar scenarios as numerical cases (Fig. 14) are also noticed in the experimental case study, as shown in Fig. 17, Table 9. The numerical case 5 (Fig. 14a) acts as a threshold for Fig. 17(a-d).

4.4.2. Damage localization step results

The experimental EWP results are shown in Fig. 18 for the identified sector results (Fig. 17 a-d). Fig. 17(b), as mentioned earlier, is a typical case where the RMSD matrix maps showed damage inside and outside the sensor network with higher value column sectors necessitating the use of a combined final step 45° sector separation scheme is used (Fig. 18c) to reduce the calculation time in localizing the damage present inside and outside the sensor network.

Analysis of Fig. 18a, which is the EWP results for data obtained from DAQR with D1 and D2 (case 1), shows the location of debonding where the ellipses intersect. This is the region of higher energy due to the intersection of the ellipses. Case 2- EWP results (Fig. 18c) show M1 inside the sensor network and D1, D2 outside the sensor network. D1, D2 and M2 from case 3 get identified in Fig. 18(e), followed by case 4 (Fig. 18g) identifying D1, D2 and M3, respectively. The threshold value is applied to sectorial Fig. 18(a, c, e, g) to show only the damage locations as shown in Fig. 18(b, d, f, h).

Table 13
Comparison table for numerical cases: grid reduction in [%], time taken (TT) in mins.

Case	Grids without sectors	Grids with EWP	Reduction in grid points	TT without sectors	TT with EWP
6	251,001	5600	97.76	12.6	4.3
7	251,001	119,856	52.24	12.8	6.9
8	251,001	89,883	64.19	12.5	6.1

4.5. Computational efficiency and accuracy of the methodology

The original debonding and mass locations with the estimation locations from EWP are estimated in the study. Table 10 shows the estimated location (centre coordinates) of EWP values, and the error estimation (ΔP) represents the difference between the estimated location and the actual location using experimental data. Table 11 shows the overall reduction in the grid points and time using experimental data. The actual centre coordinate of D1 is at (39 cm, 19.5 cm), D2 is at (15.5 cm, 28.5 cm), M1 is at (27 cm, 24 cm), M2 is at (30 cm, 33.5 cm), and M3 is at (12 cm, 12.5 cm) respectively.

Studying the values obtained from Table 10, one can see that the localization precision was good, and in the case of larger debonding (D1), the error is less than the edge length of the debonding. This proves to be handy in later NDT studies where only a short region can be scanned to verify the damages. Similar studies were also carried out for numerical cases, as shown in Table 12 and Table 13, showing good localization result values similar to experimental results. Since case 5 is a healthy model, it is not shown in the table of calculations.

The entire numerical calculations were performed using MATLAB (R2020a) on a desktop PC - Intel i7 processor with 32 GB RAM.

4.6. NDT results of the SCS

The presence of the debonding is verified using NDT - IRT and LDV methods. The IRT results verified the debondings (D1, D2) as shown in Fig. 19 with varied thermogram patterns at a particular time instance (58 s after initial heating), then plotted using MATLAB.

The IRT study served as a preliminary result and is used to cross-validate information obtained from the manufacturer. The GW full wavefield plot (Fig. 20) shows the debonding detection using waves. In the figure, the A0 mode (slower mode from the studies) detected the debonding, as the debonding has created a change in GW pattern, reflection and some interference. The debond region at the centre of the panel has changed the wave pattern, reflection and some interference of the wave. The debondings are identified at a time instance of 8.4 e-5 s.

5. Conclusions

This paper presents the ultrasonic GW propagation characteristics and a multi-step debonding assessment approach for the SCS. The study is also expanded to assess the damage (magnets) placed at various locations in the SCS. The amplitude curves obtained are based on the experimental signals that indicate the presence of multiple GW modes in the registered GW signals at 150 kHz. From the analysis of the results, the following findings are drawn.

- The presence of debonding in SCS significantly changes the amplitude of the A0 wave mode.
- This objective of the research is not only focused on the detailed assessment of the damage that is away from the actuator-sensor arrangement but also when present at a close distance, identifying multiple damages using RMSD based matrix map method, localizing the damages with reduced calculation time and grid numbers using sector-wise EWP.
- The benefit of using the damage detection step is that it allows for a quick damage check without executing velocity estimation.
- It is noticed that the RMSD matrix map values near damages are higher when compared to the cases away from the damage. The detection step helps avoid higher false-negative results in the damage localization step.
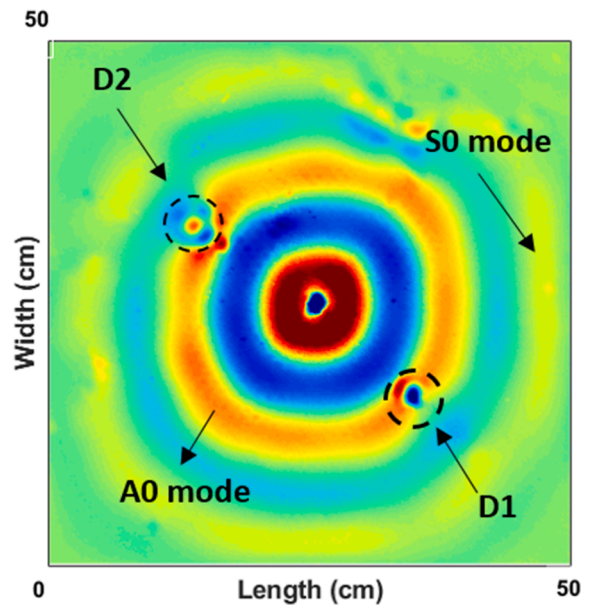
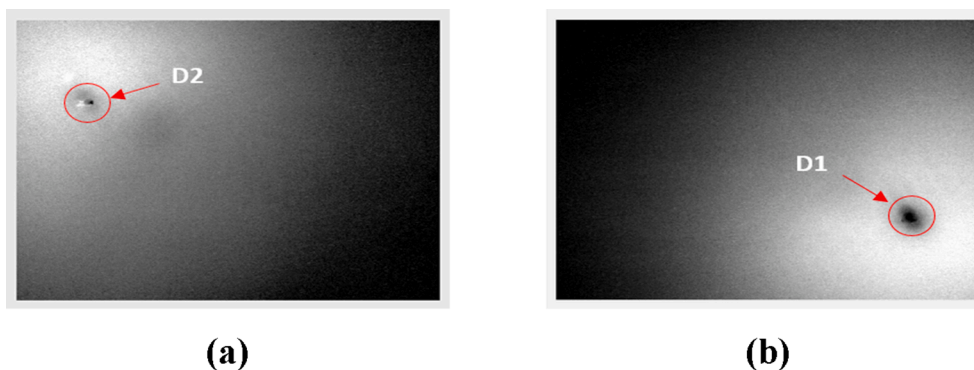**Fig. 20.** Full wavefield showing the damage locations at 150 kHz.

(a)   **(b)**

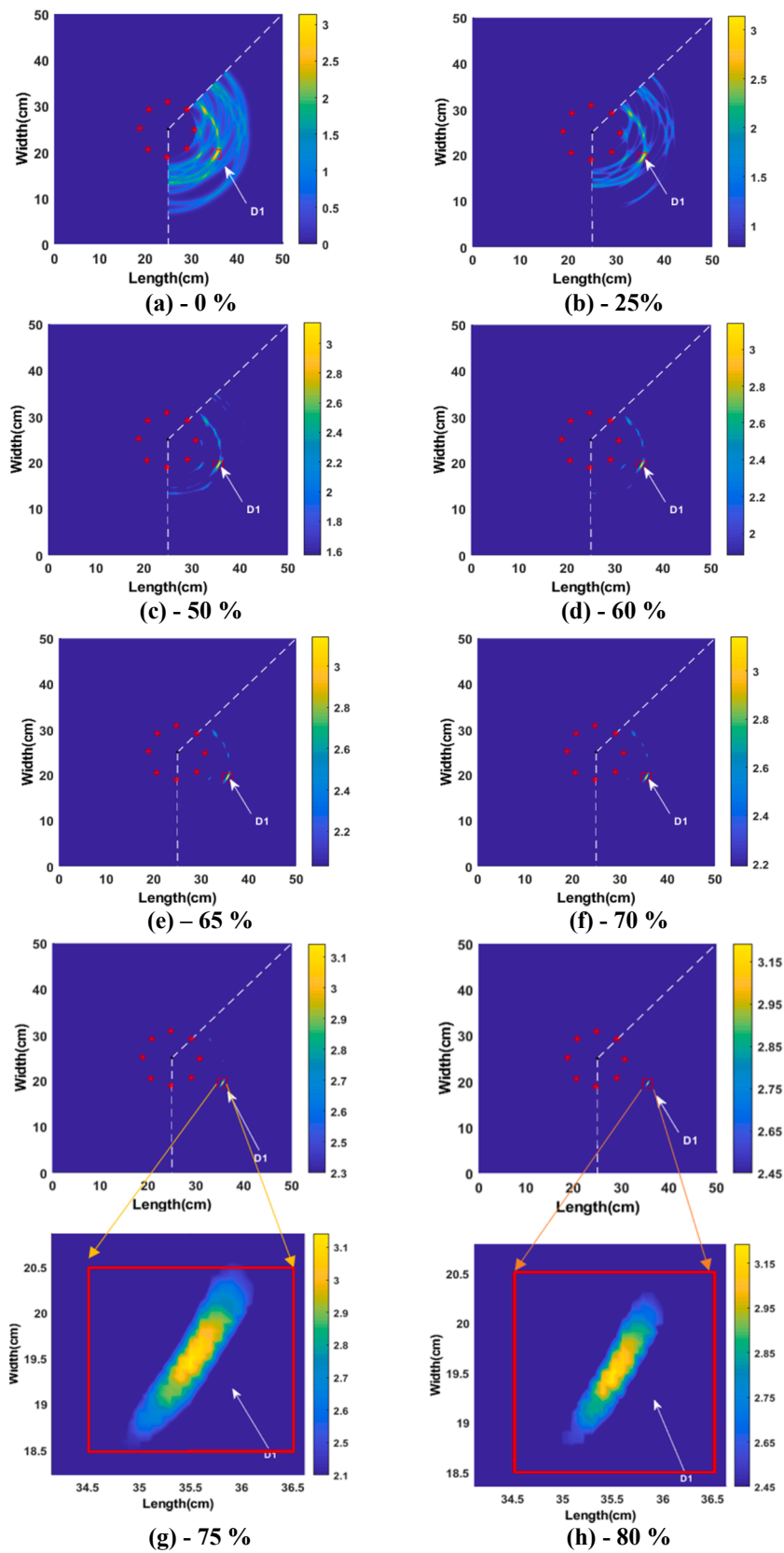**Fig. 19.** IRT thermogram results: (a) D2, (b) D1.

Fig. 21. Case 8 damage map at different percentages (thresholds).

Table 14
Pixel count based error estimation [nos = numbers].

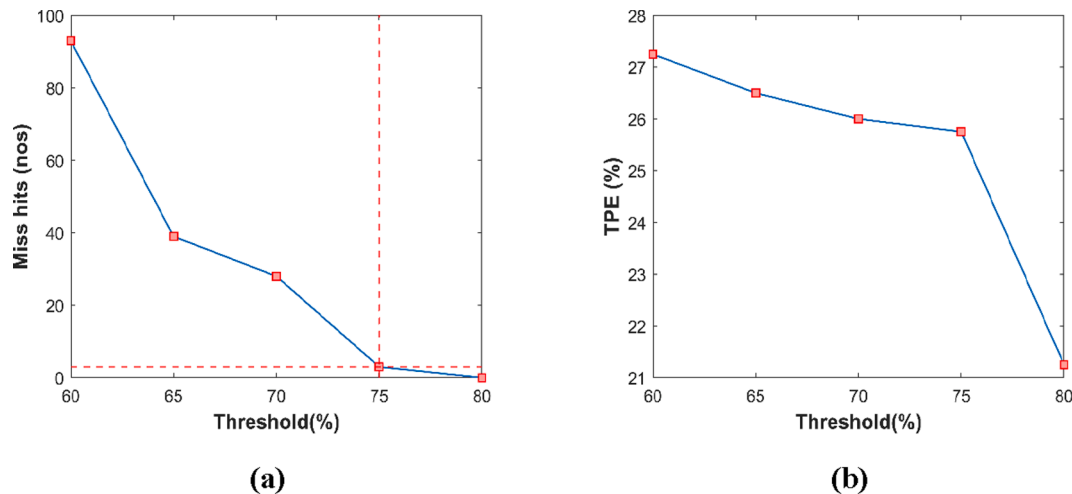| Fig. 21	D_D (Pixel nos)	Total debond EWP pixels (Pixel nos)	D_E (Pixel nos)	Miss hits estimated (Pixel nos)	TPE (%)
(a)-0 %	400	–	–	–	–
(b)-25%	400	–	–	–	–
(c)-50%	400	–	–	–	–
(d)-60%	400	202	109	93	27.25
(e)-65%	400	145	106	39	26.5
(f)-70%	400	132	104	28	26
(g)-75%	400	106	103	3	25.75
(h)-80%	400	85	85	0	21.25

Fig. 22. Threshold (vs): (a) Miss hits, (b) TPE.

- The damage detection step helped identify the damages (debonding, magnets) using both inner and outer monitoring approaches.
- Sectors (angular, circular) were created based on the detection step results later in the localization step (EWP process).
- The EWP-based SHM strategy has proven its potential to detect multiple debondings with different sizes along with multiple randomly placed mass locations in the SCS.
- Numerical models were also developed to validate the experimental modes using the proposed multi-step strategy.
- The EWP process reduced the calculation time to a maximum of 52 %, grid numbers to a maximum of 97 % and localized the damages with an error estimation value close to ~ 0.8 cm.
- The SHM results were then cross verified using the NDT methods.
- Overall benefits of the proposed SHM approach are total time reduction and fewer computations in EWP analysis due to quick sector analysis of RMSD based damage detection step.

Future research is needed based on assessing different types of damage conditions (e.g. cracks, corrosion, and delamination) with the proposed method in different types of composite structures.

CRediT authorship contribution statement

Kaleeswaran Balasubramaniam: Conceptualization, Methodology, Software, Validation, Investigation, Formal analysis, Writing – original draft, Writing – review & editing. **Shirsendu Sikdar:** Conceptualization, Methodology, Software, Validation, Writing – original draft, Writing – review & editing, Funding acquisition, Supervision. **Rohan Soman:** Conceptualization, Writing – review & editing, Supervision. **Paweł Malinowski:** Conceptualization, Software, Writing – review & editing, Funding acquisition, Supervision, Project administration.

Declaration of Competing Interest

The authors declare that they have no known competing financial interests or personal relationships that could have appeared to influence the work reported in this paper.

Acknowledgements

Appendix A1

The threshold value of 75% was taken for the damage localization based on miss-hits calculation and true positive estimation (TPE) of pixel counts shown in equation (6).

$$TPE(\%) = \frac{D_D}{D_E} \tag{6}$$

where: D_D = actual debond size (in pixel numbers) marked with a red coloured square in Fig. 21(a). In this exemplary section, case 8 (Fig. 15f) is taken, with D1 of size 20 mm × 20 mm = 400-pixel numbers, D_E = estimated size of the pixel numbers present within the D_D.

The best threshold percentage is based on the percentage at which the number of miss-hits (false predictions) are as low as possible. This indicates the pixels that correspond to damage and are considered to be detected as damaged pixels (true positive). Fig. 21 shows the various values of threshold (percentage %) plotted to check at which percentage the miss-hit values were less. The results obtained are also tabulated in Table 14, respectively.

From the figure, it can be ascertained that 75 % of the threshold (Fig. 21g) covers the D_D with the best possible D_E. Table 14 provides the error estimation based on calculating the binary pixels from threshold maps and comparing them with pixel numbers of D_D. In Table 14, Fig. 21(a-c) are omitted from the calculation for simplification purposes as the number of distributed mishits are higher.

As shown in Fig. 22(a), 80% of mishits are 0, but TPE is lower compared to its previous threshold percentage values (75% - Fig. 22b). Also, the debond pixel number inside the 80 % (Fig. 21h) is significantly lower. So, as a trade-off based on the results obtained, 75 % is chosen as the desired threshold, as it gives a low no of mishits and covers the size of the D_D with a higher number of D_E.

References

[1] V. Giurgiutiu, Structural health monitoring, Academic Press, London, 2008.

[2] S. Sikdar, W. Van Paepegem, W. Ostachowicz, M. Kersemans, Nonlinear elastic wave propagation and breathing-debond identification in a smart composite structure, Compos. B Eng. 200 (2020) 108304, https://doi.org/10.1016/j.compositesb:2020.108304.

[3] C. Li, Q. Han, Guided waves propagation in sandwich cylindrical structures with functionally graded graphene-epoxy core and piezoelectric surface layers, J. Sandwich Struct. Mater. 23 (8) (2021) 3878–3901.

[4] J. Wu, X. Chen, Z. Ma, A Signal Decomposition Method for Ultrasonic Guided Wave Generated from Debonding Combining Smoothed Pseudo Wigner-Ville Distribution and Vold-Kalman Filter Order Tracking, Shock Vib. 2017 (2017) 1–13.

[5] K. Balasubramaniam, S. Sikdar, T. Wandowski, P.H. Malinowski, Ultrasonic guided wave-based debond identification in a GFRP plate with L-stiffener, Smart Mater. Struct. 31 (1) (2022) 015023, https://doi.org/10.1088/1361-665X/ac3a97.

[6] S. Pavlopoulou, K. Worden, C. Soutis, Damage Monitoring of External Patch Repairs with Guided Ultrasonic Waves, Strain 51 (4) (2015) 288–300.

[7] H. Baid, C. Schaal, H. Samajder, A. Mal, Dispersion of Lamb waves in a honeycomb composite sandwich panel, Ultrasonics 56 (2015) 409–416.

[8] N. Chakraborty, V.T. Rathod, D. Roy Mahapatra, S. Gopalakrishnan, Guided wave based detection of damage in honeycomb core sandwich structures, NDT E Int. 49 (2012) 27–33.

[9] P.W.R. Beaumont, The Structural Integrity of Composite Materials and Long-Life Implementation of Composite Structures, Appl. Compos. Mater. 27 (5) (2020) 449–478.

[10] R. Brighenti, A. Carpinteri, D. Scorza, Mechanics of interface debonding in fibre-reinforced materials, J. Compos. Mater. 50 (19) (2016) 2699–2718.

[11] S.N.A. Safri, M.T.H. Sultan, M. Jawaid, K. Jayakrishna, Impact behaviour of hybrid composites for structural applications: A review, Compos. B Eng. 133 (2018) 112–121.

[12] L. Singher, Y. Segal, J. Shamir, Interaction of a guided wave with a nonuniform adhesion bond, Ultrasonics 35 (5) (1997) 385–391.

[13] M. Mansourinik, F. Taheri-Behrooz, The effect of interface debonding on flexural behaviour of composite sandwich beams, J. Sandwich Struct. Mater. 22 (4) (2020) 1132–1156.

[14] G. Ji, Z. Ouyang, G. Li, Debonding and impact tolerant sandwich panel with hybrid foam core, Compos. Struct. 103 (2013) 143–150.

[15] S. Mustapha, L. Ye, Propagation behaviour of guided waves in tapered sandwich structures and debonding identification using time reversal, Wave Motion 57 (2015) 154–170.

[16] L. Wang, F. Gao, Y. Zhang, L. Araque, S. Tai, B. Patel, A. Mal, An Improved Damage Index for Nondestructive Evaluation of a Disbond in Honeycomb Sandwich Structure Using Guided Waves, J. Nondestruct. Eval., Diagn. Prognost. Eng. Syst. 3 (3) (2020).

[17] R. Gorgin, Z. Wu, D. Gao, Y. Wang, Damage size characterization algorithm for active structural health monitoring using the A0 mode of Lamb waves, Smart Mater. Struct. 23 (3) (2014) 035015, https://doi.org/10.1088/0964-1726/23/3/035015.

[18] K. Balasubramaniam, P. Fiborek, S. Sikdar, P.H. Malinowski, Damage Assessment for a Sandwich-Like Panel Using Experimental and Numerical Analysis of Guided Waves, in: Advances in Non-destructive Evaluation, Springer, Singapore, 2021, pp. 73–84.

[19] J. Zhao, F. Li, X. Cao, H. Li, Wave Propagation in Aluminum Honeycomb Plate and Debonding Detection Using Scanning Laser Vibrometer, Sensors 18 (6) (2018) 1669.

[20] S. Hosseini, S. Duczek, U. Gabbert, Damage Localization in Plates Using Mode Conversion Characteristics of Ultrasonic Guided Waves, J. Nondestr. Eval. 33 (2013) 152–165.

[21] C. Schaal, A. Mal, Core-Skin Disbond Detection in a Composite Sandwich Panel Using Guided Ultrasonic Waves, J. Nondestruct. Eval., Diagn. Prognost. Eng. Syst. 1 (1) (2017).

[22] M. Castaings, B. Hosten, Guided waves propagating in sandwich structures made of anisotropic, viscoelastic, composite materials, J. Acoust. Soc. Am. 113 (5) (2003) 2622–2634.

[23] A. De Luca, D. Perfetto, G. Lamanna, A. Aversano, F. Caputo, Numerical Investigation on Guided Waves Dispersion and Scattering Phenomena in Stiffened Panels, Materials 15 (1) (2022) 74.

[24] G. Sha, H. Xu, M. Radzieński, M. Cao, W. Ostachowicz, Z. Su, Guided wavefield curvature imaging of invisible damage in composite structures, Mech. Syst. Sig. Process. 150 (2021) 107240, https://doi.org/10.1016/j.ymssp.2020.107240.

[25] M. Radzieński, P. Kudela, A. Marzani, L. De Marchi, W. Ostachowicz, Damage Identification in Various Types of Composite Plates Using Guided Waves Excited by a Piezoelectric Transducer and Measured by a Laser Vibrometer, Sensors 19 (9) (2019) 1958.

[26] S. Torkamani, S. Roy, M.E. Barkey, E. Sazonov, S. Burkett, S. Kotru, A novel damage index for damage identification using guided waves with application in laminated composites, Smart Mater. Struct. 23 (9) (2014) 095015, https://doi.org/10.1088/0964-1726/23/9/095015.

[27] V. Memmolo, N. Boffa, L. Maio, E. Monaco, F. Ricci, Damage Localization in Composite Structures Using a Guided Waves Based Multi-Parameter Approach, Aerospace 5 (4) (2018) 111.

[28] S. Sikdar, Multi-level nondestructive analysis of joint-debond effects in sandwich composite structure, Polym. Test. 80 (2019) 106149, https://doi.org/10.1016/j.polymertesting.2019.106149.

[29] M.A. Fakih, S. Mustapha, M. Makki Alamdari, L. Ye, Symbolic dynamics time series analysis for assessment of barely visible indentation damage in composite sandwich structures based on guided waves, J. Compos. Mater. 51 (29) (2017) 4129–4143.

[30] A. De Luca, D. Perfetto, A. De Fenza, G. Petrone, F. Caputo, A sensitivity analysis on the damage detection capability of a Lamb waves based SHM system for a composite winglet, Proc. Struct. Integrity 12 (2018) 578–588.

[31] D. Perfetto, A. De Luca, M. Perfetto, G. Lamanna, F. Caputo, Damage Detection in Flat Panels by Guided Waves Based Artificial Neural Network Trained through Finite Element Method, Materials 14 (24) (2021) 7602.

[32] S. Mustapha, L. Ye, Non-destructive evaluation (NDE) of composites: assessing debonding in sandwich panels using guided waves, in: *Non-Destructive Evaluation (NDE) of Polymer Matrix Composites*, Woodhead Publishing, 2013, pp. 238–278.

[33] S. Mustapha, L. Ye, D. Wang, Y.e. Lu, Debonding detection in composite sandwich structures based on guided waves, AIAA J. 50 (8) (2012) 1697–1706.

[34] S. Sikdar, W. Ostachowicz, Ultrasonic Lamb wave-based debonding monitoring of advanced honeycomb sandwich composite structures, Strain 55 (1) (2019) e12302, https://doi.org/10.1111/str.v55.110.1111/str.12302.

[35] F. Song, G.L. Huang, G.K. Hu, Online guided wave-based debonding detection in honeycomb sandwich structures, AIAA J. 50 (2) (2012) 284–293.

[36] K. Balasubramaniam, P. Fiborek, D. Ziaja, M. Jurek, M. Sawczak, R. Soman, P. H. Malinowski, Global and local area inspection methods in damage detection of carbon fiber composite structures, Measurement 187 (2022) 110336, https://doi.org/10.1016/j.measurement.2021.110336.

[37] J.E. Michaels, T.E. Michaels, Guided wave signal processing and image fusion for in situ damage localization in plates, Wave Motion 44 (6) (2007) 482–492.

[38] C. Fendzi, N. Mechbal, M. Rébillat, M. Guskov, G. Coffignal, A general Bayesian framework for ellipse-based and hyperbola-based damage localization in anisotropic composite plates, J. Intell. Mater. Syst. Struct. 27 (3) (2016) 350–374.

[39] K. Balasubramaniam, S. Sikdar, P. Fiborek, P. Malinowski, Ultrasonic Guided Wave Signal Based Nondestructive Testing of a Bonded Composite Structure Using Piezoelectric Transducers, Signals 2 (1) (2021) 13–24.

[40] Ceramtec.com. 2021. *CeramTec – The Ceramic Experts*. [online] Available at: <https://www.ceramtec.com/> [Accessed 28 October 2021].

[41] P. Malinowski, T. Wandowski, W. Ostachowicz, Damage detection potential of a triangular piezoelectric configuration, Mech. Syst. Sig. Process. 25 (7) (2011) 2722–2732.

[42] G. Giridhara, V.T. Rathod, S. Naik, D. Roy Mahapatra, S. Gopalakrishnan, Rapid localization of damage using a circular sensor array and Lamb wave based triangulation, Mech. Syst. Sig. Process. 24 (8) (2010) 2929–2946.

[43] T. Wandowski, P.H. Malinowski, W.M. Ostachowicz, Circular sensing networks for guided waves based structural health monitoring, Mech. Syst. Sig. Process. 66-67 (2016) 248–267.

[44] G. Sha, R. Soman, M. Radzieński, M. Cao, W. Ostachowicz, H. Zuo, A two-step method for additional mass identification in beam structures by measurements of natural frequencies and guided waves, Measurement 186 (2021) 110049, https://doi.org/10.1016/j.measurement.2021.110049.

[45] Flir.eu. 2021. *Thermal Imaging, Night Vision and Infrared Camera Systems | Teledyne FLIR*. [online] Available at: <https://www.flir.eu/> [Accessed 25 October 2021].

[46] Y. He, B. Gao, R. Yang, A. Sophian, Transient electromagnetic-thermal nondestructive testing, Elsevier, 2017.

[47] S. Sikdar, P. Mirgal, S. Banerjee, W. Ostachowicz, Damage-induced acoustic emission source monitoring in a honeycomb sandwich composite structure, Compos. B Eng. 158 (2019) 179–188.

[48] T. Wang, *Finite element modelling and simulation of guided wave propagation in steel structural members*, Doctoral dissertation, University of Western Sydney (Australia), 2014.

[49] J.R. Vinson, R.L. Sierakowski, The behavior of structures composed of composite materials, Springer, 2006.

[50] M.S. Hoo Fatt, K.S. Park, Dynamic models for low-velocity impact damage of composite sandwich panels – Part A: Deformation, Compos. Struct. 52 (3-4) (2001) 335–351.

[51] L. Yu, Z. Tian, X. Li, R. Zhu, G. Huang, Core–skin debonding detection in honeycomb sandwich structures through guided wave wavefield analysis, J. Intell. Mater. Syst. Struct. 30 (9) (2019) 1306–1317.

[52] P. Fiborek, P. Kudela, W.M. Ostachowicz, 2D–3D interface coupling in the time domain spectral element method for the adhesive layer effects on guided wave propagation in composite plates, Smart Mater. Struct. 28 (5) (2019) 055014, https://doi.org/10.1088/1361-665X/ab0b69.